Continuous-Flow Electrokinetic-Assisted Plasmapheresis by Using Three-Dimensional Microelectrodes Featuring Sidewall Undercuts

Xiaoxing Xing,[†] Minghao He,[‡] Huihe Qiu,[‡] and Levent Yobas[*,†,§]

[†]Department of Electronic and Computer Engineering, [‡]Department of Mechanical and Aerospace Engineering, and [§]Division of Biomedical Engineering, The Hong Kong University of Science and Technology, Clear Water Bay, Hong Kong SAR, China

S *Supporting Information*

ABSTRACT: We present a novel plasmapheresis device designed for a fully integrated point-of-care blood analysis microsystem. In the device, fluidic microchannels exhibit a characteristic cross-sectional profile arising from distinct three-dimensional (3D) microelectrodes featuring sidewall under-cuts readily integrated through a single-mask process. The structure leverages mainly electrothermal convective rolls that efficiently manifest themselves in physiological fluids and yet have received inadequate attention for the application of plasmapheresis due to concerns over Joule heating. Using this device, we show that such convective rolls not only lead to plasma extraction at a high yield and purity but also deliver plasma at an acceptable quality with no evidence of hemolytic stress or protein denaturation. Specifically, plasma from 1.5 μL of whole blood diluted to 4% hematocrit in a high-conductivity buffer (1.5 S/m) is extracted in a continuous flow at a fraction of 70% by using a peak voltage of ± 10 V$_p$ applied at 650 kHz; the extracted plasma is nearly 99% pure, as shown by a rigorous assessment using flow cytometry. The plasmas obtained using this device and using conventional centrifugation and sedimentation are of comparable quality as revealed by absorbance and circular dichroism spectra despite thermal gradients; however, these gradients effectively drive electrothermal bulk flows, as assessed using the microparticle image velocity technique. The device achieves high target molecule recovery efficiency, delivering about 97% of the proteins detected in the plasma obtained using sedimentation. The utility of the extracted plasma is further validated based on the detection of prostate-specific antigen at clinically relevant levels.
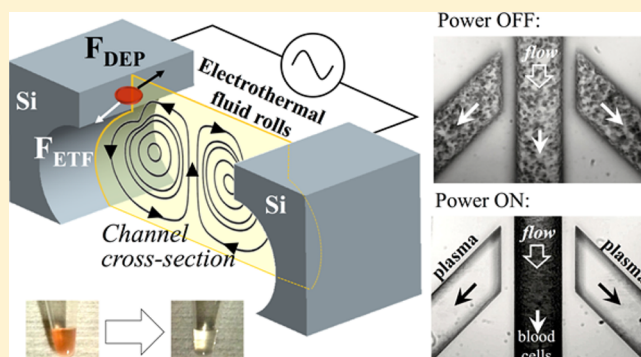
Plasma, the straw-colored liquid that accounts for approximately 55% of total blood volume, presents a host of biomarkers such as proteins, metabolites, circulating nucleic acids, and pathogens.[1] Effective detection of these biomarkers depends on the isolation of cell-free plasma from blood, which is commonly achieved using, for example, centrifugation or filtration, although these methods are affected by limitations such as being labor-intensive and prone to human error.[2] Nevertheless, recent methodological developments for blood plasma separation are increasingly focused on microfluidic techniques; the objective here is to miniaturize and integrate all the steps of blood plasma analysis into a compact system, and this is driven mainly by the vision of point-of-care tests.[3]

Microfluidic techniques used for isolating blood plasma cover various passive mechanisms, including gravity (sedimentation),[4] size exclusion (filtration),[5] and cell deviation.[6] Sedimentation, which relies on gravity and on density contrasts across blood constituents, is a slow process, and its throughput is low unless combined with weirs or trenches.[7] Filtration through micro-fluidic sieves features a sharp cutoff size, owing to a highly regular pore array defined using semiconductor process technologies,[8] but much like traditional track-etched membranes, these filters are affected by clogging unless measures are

taken against clogging and subsequent pressure buildup that leads to hemolysis.[9] Cross-flow filtration, where the flow is applied tangentially rather than directly to the sieve, mitigates clogging and retards sieve saturation.[10] The drawback can be further eased by adopting a large critical gap across post arrays or slanted barriers such that cells are deviated until they are cleared off, as in deterministic lateral displacement (DLD)[11] or hydrophoresis.[12] However, because the size of these gaps must be comparable to that of the average cell, large cells or cell clusters cannot pass through the gaps. The lateral migration of cells due to viscous lift forces leaves a cell-free layer across microchannels, which can be branched off downstream (plasma skimming),[13] and blood plasma can also be skimmed by exploiting the tendency of cells at a bifurcation to enter the branch featuring a higher flow rate (the Zweifach–Fung effect).[14] However, these methods frequently compromise purity over yield or vice versa. Although the inertial migration of cells in microchannels leads to a clog-free operation, this might not represent an optimal choice for the envisioned

integrated plasma analysis system because the samples must be highly diluted to lower the hematocrit (Hct) level and applied in large volumes at high flow rates to engage inertial forces.[15]

Active microfluidic techniques for blood plasma separation involve external force fields (e.g., acoustic,[16,17] magnetic,[18] and electric fields[19−21]) and provide a clog-free operation, which is compatible with integrated blood plasma analysis. Among those, electrical separation of blood plasma, despite presenting favorable characteristics for a fully integrated blood analysis system, has been explored only recently.[19−21] Nakashima et al.[19] used a thin-film microelectrode pattern to apply dielectrophoretic (DEP) forces in order to clear blood cells off the entrance of microchannels and thus allow plasma to be freely collected under the capillary effect. The plasma yield was reported as 6% (300 nL isolated from 5 μL of 1:9 diluted blood), and the purity achieved was 98%. Jiang et al.[20] employed wire electrodes placed externally in reservoirs to induce electroosmotic flows that caused a fraction of blood plasma to be drawn into bifurcation channels that were held under a weaker electric field than the supply channel and were thus unable to attract cells from the supply stream. Although very few blood cells were observed entering the plasma channels, the plasma yield was found to remain below 26% based on the processing of 500 nL of 1:16 diluted blood. Chen et al.[21] placed thin-film electrodes on a pair of glass slides and thus had the electric field capacitively coupled into a channel sandwiched between the assembled pair; as blood was drawn into the channel under capillary action, cells appeared polarized and began to aggregate due to dipole−dipole interactions induced by a weak electric field. The aggregates were retained, whereas plasma from undiluted whole blood continued to fill the channel and reached a yield and purity of nearly 70% and 89%, respectively. These studies have drawn attention to the benefits that an electrical approach offers to plasmapheresis, but explored only the principles of dielectrophoresis and electro-osmosis among electrokinetic phenomena.

Here, we report a continuous-flow separation of blood plasma based on electrokinetic forces in a microfluidic device. Unlike the previously described devices in which separation occurs mainly through dielectrophoresis or electroosmosis, which are typically effective with low-conductivity fluids or with sharply defined potential wells,[22] our plasmapheresis device engages primarily the principle of electrothermal flow (ETF). ETF, an electrohydrodynamic effect, persists over a broad conductivity range and is particularly effective with physio-logical fluids such as blood plasma, which commonly exhibit high conductivity (>1 S/m).[23] Studies conducted to date have exploited electrothermal effects in high-conductivity media largely to enhance the sensitivity and temporal response of heterogeneous immunoassays[24,25] as well as electrochemical biosensors,[26,27] the DEP manipulation and trapping of colloidal particles[28] or bacteria,[29] and the DEP trapping and isolation of human breast adenocarcinoma cells from leucocytes.[30] However, to the best of our knowledge, no published report has described the use of ETF for blood plasma extraction and presented analytical measurements verifying the quality and utility of the extracted plasma. A summary of state-of-the-art microfluidic plasmapheresis devices stating their key operation principles as well as various other features is provided in Supporting Information (Table S-1).

Figure 1 illustrates the device concept. A unique feature of our device is that it employs a pair of opposing three-dimensional (3D) silicon electrodes fabricated with sidewall
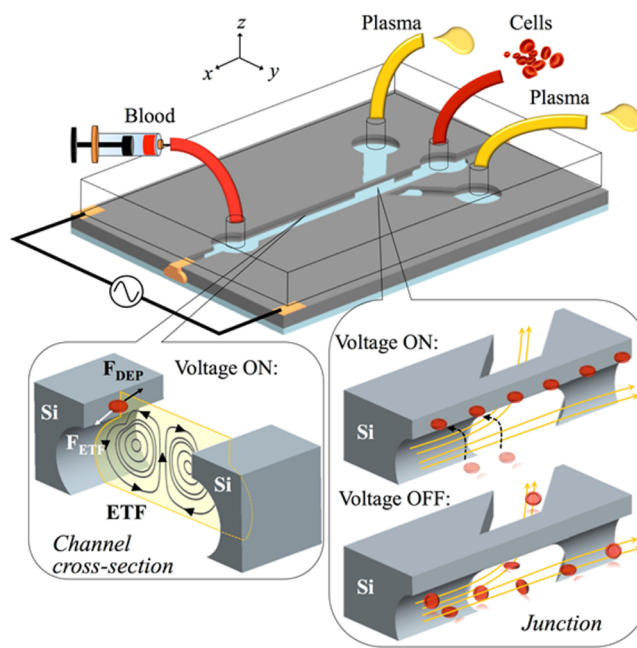
Figure 1. Three-dimensional renderings of the device. A straight flow channel is situated between a pair of opposing 3D silicon electrodes designed with sidewall undercuts that lead to bridges at a downstream junction where plasma is branched off from blood cells. When a sufficient voltage is applied, blood cells are levitated and enriched in the upper channel layer under the combined effect of ETF (fluid rolls, left inset) and DEP forces and thus prevented from entering the side branches by the respective electrode bridges located at the junction (right inset).

undercuts by tailoring a silicon dry-etch profile through a single-mask photolithography process.[31,32] We previously introduced such electrodes in the construction of an interdigitated comb array and separated cells under DEP forces in the batch mode.[33−35] Here, we used these electrodes to construct a comparatively simple device that performs continuous-flow separation of blood plasma. In this design, a straight channel (100 μm wide, 75 μm deep, and about 30 mm long) extends from a single inlet to a downstream junction where it branches out into daughter channels that terminate at distinct outlets. The junction features a bridge on either side that is simply a monolithic extension of the respective 3D silicon electrode. These bridges are crucial for preventing blood cells from entering the side branches after the cells are levitated to the bridge level under secondary bulk flows due to electrothermal effects and confined within upper streams under DEP forces (Figure 1, inset diagrams). Thus, as blood cells proceed to the center outlet, they are enriched in the upper streams and partitioned from the cell-depleted clear plasma that constitutes the bottom streams that readily fractionate into side branches.

EXPERIMENTAL SECTION

Computations. Simulations were performed using COM-SOL Multiphysics software v4.3 (Comsol Inc., Burlington, MA) according to the theory and numerical procedure detailed in Supporting Information.

Device Fabrication. The devices were built on a 100 mm silicon-on-insulator (SOI) substrate at a thickness of 75, 2, and 500 μm for the device, buried oxide, and handle layers, respectively. On the substrate, an aluminum (Al) film was

sputtered at a thickness of 400 nm and then patterned by dry etching through a resist mask. The device layer was structured partially with the channel layout through a SiO_2 hard mask in a deep reactive ion etching (DRIE) step. A thin film of tetraethylorthosilicate (TEOS) was deposited on the entire topography and then removed from the channel floors by using an anisotropic etch. With the channel sidewalls masked under TEOS, the silicon bulk exposed on the channel floors was removed in SF_6 plasma, which resulted in the formation of sidewall undercuts and junction bridges. This step also created entirely isolated silicon blocks, i.e., the electrodes, and exposed the buried oxide layer on the channel floors. After dicing the substrate into discrete devices, the channel layout in each device was enclosed from above using a thin poly-(dimethylsiloxane) (PDMS) slab punched with fluidic access ports and electrical vias. Both the device and the PDMS slab were surface activated in oxygen plasma to ensure irreversible bonding. The TEOS covering the electrical vias was removed using hydrofluoric acid applied locally to create access to the Al thin films. Lastly, the device was mounted on a custom printed circuit board (PCB) by using a double-sided adhesive tape, and the electrical contacts were established by securing copper wires to the electrodes by using silver colloidal paste (Ted Pella, Inc., Redding, CA).

Blood Samples. Human whole blood was freshly drawn from healthy donors through venipuncture into VACUETTE EDTA (ethylenediaminetetraacetic acid) tubes (Greiner Bio-One International, GmbH, Frickenhausen, Germany). Blood samples were stored at 4 °C and used within 48 h. Before use, the samples were diluted at a ratio of 1:9 with 1× phosphate-buffered saline (PBS) at a conductivity of 1.5 S/m (composition, in mM: 136.89 NaCl, 2.68 KCl, 1.47 KH_2PO_4, and 8.10 Na_2HPO_4; pH 7.4). To prepare low-conductivity samples, the dilution was performed with 300 mM D-mannitol (conductivity: 2×10^{-4} S/m), and the conductivity was adjusted to either 100 or 10 mS/m by using PBS.

Plasmapheresis. The devices were prepared for plasmapheresis by coating with 5% BSA−PBS for 1 h and then rinsing with PBS. However, the coating step was omitted if the collected fractions were to be analyzed for protein denaturation, total protein recovery yield, or target protein concentration. For each run, the device was placed on the stage of an upright microscope (Nikon Eclipse, FN1; Nikon, Tokyo, Japan) equipped with a CCD camera (RT3Mono, SPOT Imaging, Sterling Heights, MI). For voltage activation, the device was connected to a function generator (CFG250, Tektronix, Beaverton, OR) through a transformer and power amplifier (AL-50HFA, Amp-Line Corp., West Nyack, NY). The activation peak and frequency were monitored on an oscilloscope (TDS2012C, Tektronix). A piece of Tygon tubing containing the blood sample to be processed was inserted into the device inlet port and connected to a 1 mL syringe (BD Tuberculin, Becton, Dickinson and Co., Franklin Lakes, NJ) driven by an infusion pump (Harvard Apparatus, Holliston, MA). The sample was delivered into the device at a controlled flow rate upon voltage activation until an aliquot of 15 µL was completely processed. The fractions of the enriched cells and extract were collected into separate pieces of Tygon tubing inserted into the respective outlet ports and they left vented to the atmosphere. The collected fractions were stored at 4 °C until further analysis. For comparison, this experiment was repeated under identical conditions but with the voltage activation turned off. For further comparison, plasmapheresis

was also conducted by using conventional methods to process 1 mL of the same blood sample: samples were centrifuged at 1500g for 5 min or allowed to sediment in a 4 °C refrigerator for 2 h. The supernatant was carefully aspirated using a pipet, and the fraction reaching at least 1 mm above the cell pellet was left uncollected in order to avoid cell contamination. The extracts were all stored on ice until further evaluation.

Measurements. ETF velocity and steady-state temperature within the device channel under an applied activation voltage were measured through the microparticle image velocity (µPIV) and fluorescence-based thermometry techniques, respectively. The collected fractions were analyzed for yield and purity, hemolysis and protein denaturation, total protein recovery yield, and target protein recovery. These procedures are detailed in Supporting Information.

■ RESULTS AND DISCUSSION

Device Architecture. Figure 2a shows scanning electron microscopy (SEM) images from a representative device without
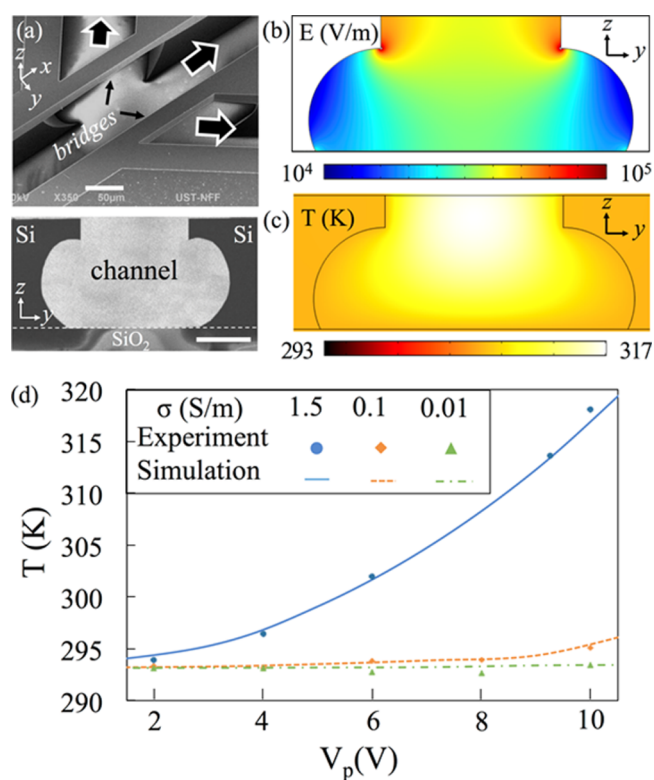
Figure 2. (a) SEM images: upper panel, oblique view of the junction; lower panel, cross-sectional view of the main channel at a site away from the junction. Scale bar: 50 µm. (b) Electric field and (c) thermal field simulated across the main channel with the stagnant aqueous content at 1.5 S/m. Activation: ± 10 V_p at 650 kHz. (d) Plots of the peak voltage vs the temperature simulated and measured at various conductivities of the channel aqueous content (legend). No external pressure was applied.

a cover slab. The device junction at which blood plasma is separated from cells is depicted from an oblique view (upper panel). The bridges held by the respective silicon electrodes on either side of the junction are intact and appear structurally robust. The electrodes feature a sidewall undercut that also defines the shape of the flow channels, as shown in a cross-sectional view of the main channel at a site away from the

junction (lower panel). The channels are uniformly wide—100 μm—along their initial depth (17 μm), but thereafter expand to a width of 160 μm. The upper channel layer becomes filled with blood cells that are enriched under electrothermally driven secondary bulk flows as the cells are transported under pressure-driven flow to the downstream junction situated 24 mm from the inlet port. Thus, levitated cells bypass the side channels because the junction bridge blocks passage on either side. This channel layer accounts for a fraction (<50%) of the total volume in relation to the lower layer and presumably becomes saturated with cells at full capacity; consequently, blood must be diluted for an effective plasmapheresis.

Electric and Thermal Fields. Parts b and c of Figure 2, respectively, show simulated electric and thermal fields across the channel at a liquid conductivity of 1.5 S/m and a peak voltage of ± 10 V$_p$ delivered at 650 kHz (see Figure S-1 and Table S-2). As expected, the electric field intensity is higher near the linear segment of either sidewall than near the curved segment (the undercut), and the intensity peaks around the site where the two segments meet. By contrast, the thermal profile features a maximum in the channel center that is closer to the linear segments between the sidewalls than to the curved segments. For the aforementioned conductivity and peak voltage, the liquid temperature rises above the ambient temperature by a maximum of approximately 24 K. As shown in Figure 2d, the temperature of the liquid also exhibits a quadratic variation with the peak voltage in accordance with eq 3 (Supporting Information). The simulations (fittings) agree closely with the fluorescence-based thermometry readings from the device (symbols). The temperature variation appears markedly larger for the liquid used here at a high conductivity than for the low-conductivity liquids commonly used for electrokinetic applications (e.g., 100 and 10 mS/m). The thermal gradient, although sufficient for inducing convective ETF rolls, raises concerns regarding hemolysis or protein denaturation. This motivated us to further investigate the quality of the plasma extracted by the device.

ETF Effectiveness. Given the unique profile of the 3D electrodes, the strength and trajectories of ETF across the channel were investigated using simulations and experiments (under conditions that were otherwise stagnant; i.e., no pressure-driven flow). Figure 3a shows the simulated trajectories of 1 μm particles seeded evenly across the channel at buffer conductivity of 1.5 S/m and under an activation voltage of ± 10 V$_p$ at 650 kHz. These trajectories describe a pair of convective fluid rolls circulating symmetrically in opposite directions as predicted by the theory (Supporting Information). Because the Coulombic force dominates, i.e., $\omega\tau \ll 1$, eq 1 (Supporting Information) is reduced to $\langle \mathbf{f_E} \rangle \sim -(\nabla T \cdot \mathbf{\bar{E}})\mathbf{\bar{E}}$ and the directions of the streamlines can be accordingly understood in light of the electric field intensity ($\mathbf{\bar{E}}$) and temperature (T) profiles presented in Figure 2. The numerically simulated flow patterns and those obtained empirically from μPIV measurements (lower panel, Figure 3a; Supporting Information, Movie I) also show acceptable agreement in intensity, both being within the same order of magnitude. The measurements at various segments along the channel suggest that the fluid rolls are reasonably homogeneous (Figure S-2). The slight deviation from the axial symmetry in μPIV measurements could be attributed to inherent errors that arise from finite tracer particle numbers, sample volume size, and image resolution.[36] To further establish the electrothermal origin of the fluid rolls, average particle velocity was measured for a random set of
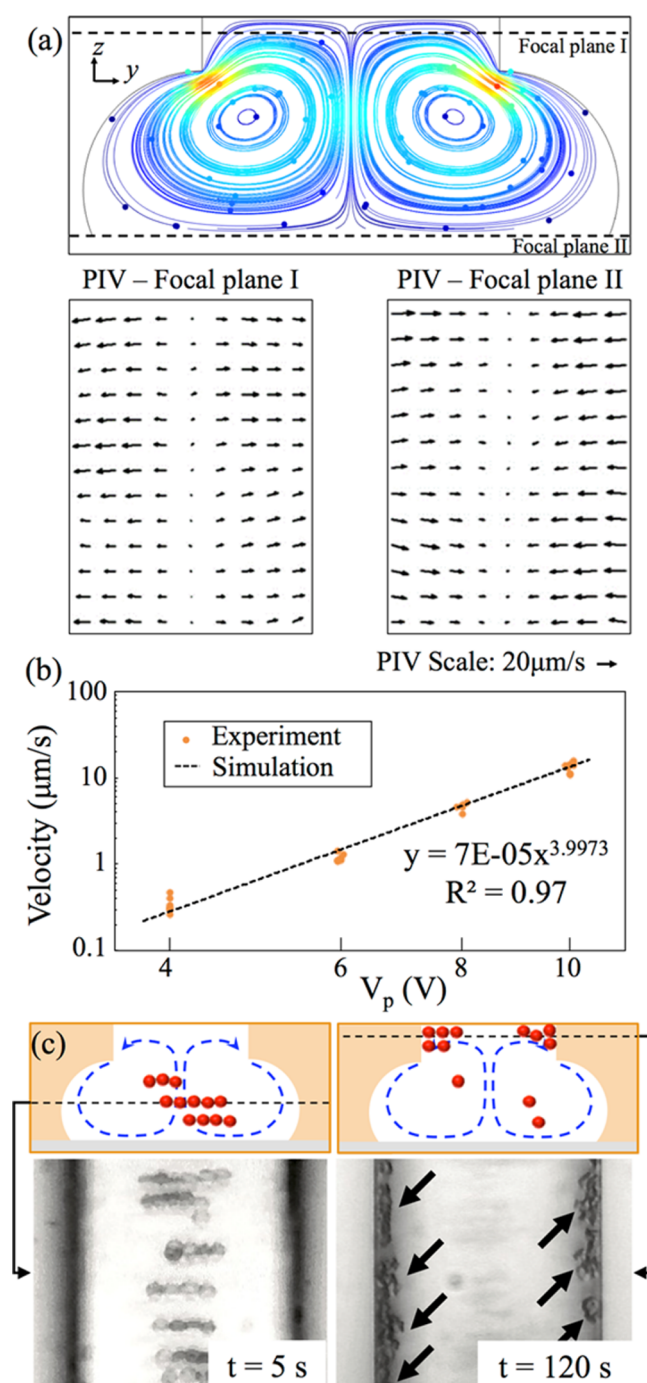
Figure 3. ETF across the channel (aqueous content 1.5 S/m) at the junction upstream. No external pressure was applied. Activation: ± 10 V$_p$ at 650 kHz unless otherwise stated. (a) Simulated trajectories color-coded for speed, ranging from red (150 μm/s) to blue (4 μm/s), and fluid velocity fields obtained from μPIV measurements. (b) Log−log plot of the peak voltage vs single-particle average velocity. (c) Qualitative descriptions of blood cell trajectories based on the accompanying images captured at 5 and 120 s after the onset of the peak voltage of ± 5 V$_p$ applied at a frequency of 650 kHz. Hct 0.5% after dilution in PBS at 1.5 S/m. The dashed lines denote the focal planes for which corresponding μPIV measurements and images are presented.

particles ($n > 5$) and plotted against the applied peak voltage (Figure 3b). The relation that emerged from the curve fitting ($R^2 = 0.97$) is nearly quartic in accordance with the ETF theory.

The simulations also suggest that the fluid rolls are insensitive to ambient temperature although the peak temperature inside the channel can show a noticeable variation when all the thermal boundary conditions are allowed to follow ambient temperature (Figure S-3).

The ETF effectiveness was also investigated on blood cells under similar conditions but at a lower peak voltage (± 5 V_p at 650 kHz). To trace single cells, the hematocrit was lowered (0.5%) by diluting blood in PBS at a conductivity of 1.5 S/m. Upon the voltage onset (Supporting Information, Movie II), the cells appeared to form "pearl chains" positioned toward the channel center, where the field intensity is weak (left panel, Figure 3c). Subsequently, the cells were levitated and enriched and they formed a band near either sidewall (arrows; right panel, Figure 3c). The cell levitation implied a translation against the electric field gradient, which suggests that the ETF drag forces had overtaken the local negative DEP (nDEP) forces. However, once the cells reached the sidewalls, they were unable to follow the fluid rolls partly because of the strong local nDEP forces pushing them away from the electrode edges between the linear and curved segments. As the peak voltage was increased, the number of cells levitated and enriched near the sidewalls was increased (not shown). However, the lack of an optimal peak voltage above which cells could start escaping signified the stagnant nature of the upper channel layer (i.e., the presence of a weak local ETF drag despite the quartic increase with the peak voltage).

Experiments were also conducted at reduced activation frequencies while maintaining the peak voltage at ± 5 V_p. Intriguingly, with the reduced activation frequency, both the nDEP force and ETF drag were found greatly weakened; blood cells were weakly polarized in pearl chains that remained mostly scattered across the channel, while only a few cells could be raised to the sidewalls (Figure S-4a). Increasing the peak voltage did not noticeably improve this situation. This was initially unexpected but later found consistent with a simple frequency analysis taking into account the electrode contact impedance and double layer capacitance; the voltage fraction across the sample declines for the peak voltage applied at reduced frequencies as the voltage fraction across the contact impedance and the double layer capacitance both rise (Figure S-4b). A similar account was also reported for a previous design whereby ETF was applied to stir proteins in a diffusion-limited heterogeneous assay;[25] the ETF velocity at 200 kHz was found more than an order of magnitude smaller than the predicted value, and this led the authors to adopt an effective voltage across the channel that was significantly lower than the applied magnitude to reconcile their results. To avoid this issue here, subsequent experiments were performed at 650 kHz.

Separation of Blood Plasma. A parametric study was undertaken to determine the hematocrit level and flow rate to achieve an effective plasmapheresis. In these experiments, the device junction was monitored and the separation effectiveness was qualitatively evaluated based on the observed cell escapes into the side branches. For undiluted whole blood (Hct $\sim$40%), the device activation showed no separation for the peak voltages up to 10 V_p and the flow rates down to 0.05 mL/h. Higher peak voltages and lower flow rates were avoided to restrict the sample exposure to excess heat and retain a practical plasmapheresis time. Subsequent experiments were conducted using progressively lower hematocrit levels with the whole blood samples diluted in PBS at a conductivity of 1.5 S/m (Figure S-5). An acceptable separation was reached at 4% Hct,

which corresponds to a dilution ratio of 1:9, when using the peak voltage of 10 V_p while keeping the flow rate of 0.05 mL/h. Under these conditions, cell escapes can be rarely observed as depicted in Figure 4a (left panel). The main channel is shown
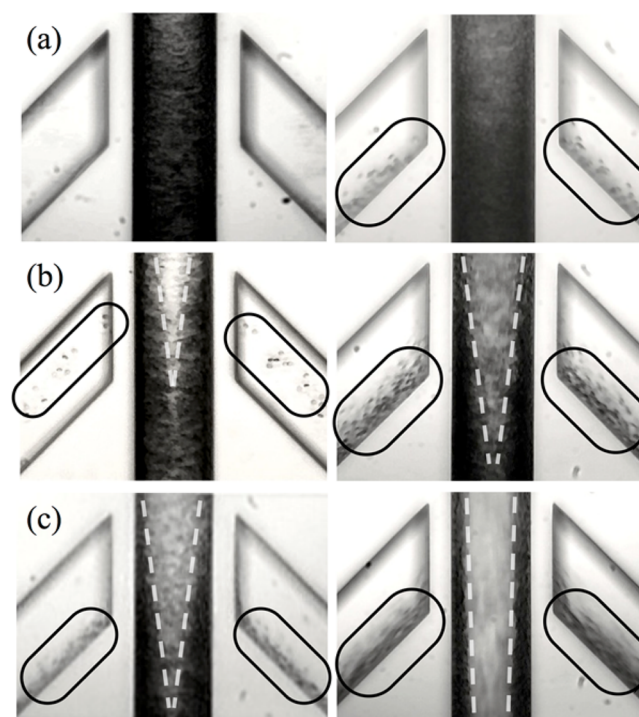
Figure 4. Plasma extraction in the device from a blood sample injected at a constant flow rate: (a) 0.05, (b) 0.1, or (c) 0.15 mL/h. Still images depicting the device junction during the extraction performed at a constant peak voltage (left panel, 10 V_p; right panel, 7.5 V_p) delivered at 650 kHz. Hct 4% after dilution at a ratio of 1:9 in PBS at 1.5 S/m. With increased flow rates ($>$0.05 mL/h) or reduced peak voltages ($<$10 V_p), cells begin escape to the side branches (encircled regions). Cells remaining in the main branch become levitated and enriched in the upper channel layer forming a dark band that expands (dashed lines) while migrating downstream.

as being completely occupied with blood cells, which suggests that the cells were effectively levitated and enriched in the upper channel layer (the image focal plane) and thus prevented by the electrode bridges from entering the side branches (Supporting Information, Movie III).

Figure 4 also shows the device junction with a reduced activation peak voltage at 7.5 V_p and increased flow rates at 0.1 and 0.15 mL/h. For the increased flow rates, the main channel is shown comparatively less occupied with cells and cells can be seen mostly scattered (below the focal plane) except near either electrode bridge where they can be observed enriched, forming a narrow band that expands while migrating downstream (dashed lines). This signifies that these increased flow rates rendered the combined action of ETF drag and nDEP force less effective for levitating and retaining cells in the upper channel layer, thereby causing the observed cell escapes to the side branches (encircled regions). The characteristic expansion of the band of enriched cells along either electrode is due to the flow splitting effect at the junction causing the flow rate to drop and allowing the ETF drag and nDEP force to regain significance in levitating and retaining cells in the upper channel layer. This is in agreement with the apparent expansion

of the bands becoming less dramatic with the increased flow rate and reduced peak voltage.

To enable plasmapheresis from whole blood at a normal hematocrit level without dilution, the device cross-sectional profile needs to be optimized. This is worthwhile only if the utility of the plasma obtained by this method including its purity and quality can be demonstrated. In the remaining, we address this issue by presenting results from a set of analytical measurements performed on the device extracts. All the device extractions were performed by injecting a 15 μL aliquot of whole blood samples (diluted at a ratio of 1:9 in PBS at 1.5 S/m to obtain Hct ~4%) at 0.05 mL/h while applying 10 V_p at 650 kHz. Plasmas were collected at a yield of 70.4% ± 2.8% (n = 4) typically within a duration of ~20 min. It should be noted that the yield and purity evaluations are independent of the dilution ratio because the fraction collected as "plasma" reflects the same level of dilution (1:9); the dilution ratio gets canceled out in the calculations. These evaluations, along with various other features, are compared against those reported for state-of-the-art microfluidic plasmapheresis devices in Table S-1. It should be further noted that the device targets a point-of-care biomarker detection microsystem to analyze a small volume of blood sample for critical diseases such as cancer by leveraging specifically label-free ultrasensitive nanobiosensors (e.g., silicon nanowires), which is proven to be powerful for rare biomarker detection and shares a similar fabrication process (DRIE) and substrate type (SOI).[37]

Purity of the Extract. Purity was assessed based on the precise count obtained for blood cells by using a flow cytometer. Figure 5a displays the dot plots of the forward-
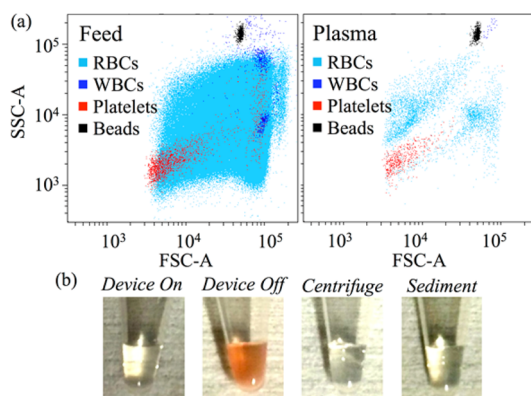
Figure 5. Purity. (a) Representative dot plots of FSC and SSC data from the feed sample (Hct 4% after dilution at a ratio of 1:9 in PBS at 1.5 S/m) and the fraction extracted by using the device (±10 V_p at 650 kHz; 0.05 mL/h). (b) Photographs of tubes containing the extracts obtained by using the device (with voltage on and off) and using centrifugation and sedimentation.

scattered (FSC, particle size) versus side-scattered (SSC, particle granularity) data for a typical sample feed and the fraction extracted using the device. The plots also show the high side-scattered data for 10 μm fluorescent beads used as reference particles (total: 1000). The sample feed contained 97.2% red blood cells (RBCs), 0.11% white blood cells (WBCs), and 2.7% platelets, all within their normal physiological range. RBCs, which are discoid, show a broader distribution in size and granularity as compared to the other cells and bridge the platelet and WBC clusters that occupy the lower left and upper right quadrants, respectively. WBCs are

uniform in size but show scatter in granularity because of being nucleated. A small platelet cluster overlaps WBCs and is considered to represent aggregates. The device extract was substantially depleted of large cells, including WBCs, RBCs, and platelet aggregates. Small platelets and RBCs could not be removed any further potentially because they faced a weak nDEP force that was insufficient for countering the ETF drag and retaining these cells in the upper layer.

The result in Figure 5a indicates that the extracted fraction was 99.35% pure, based on the accepted definition $1 - (c_p/c_f)$, where c_p and c_f refer to the RBC density in the harvested and the feed fractions, respectively. This purity level is based on the c_p value measured as 3.7×10^6 per mL (sample 1 in Table S-3). On average, the harvested fraction contained $5.3 \pm 1.1 \times 10^6$ RBCs/mL (n = 4; Table S-3) corresponding to a purity of 98.9% ± 0.3%. However, to evaluate the influence of electrokinetic effects on the purity even more rigorously, the RBCs that sediment in the feeding tube and collection reservoirs during the process must be considered (see Figure S-6 for the sediments in the reservoirs and Figure S-7 and Table S-3 for a detailed breakdown analysis). When the sediments were considered, the purity dropped slightly (to 98.5% ± 0.3%; n = 4). Moreover, the results in Table S-3 showed that 80.1% ± 8.2% of RBCs were actively removed at the junction, a substantial increase compared to 33.0% ± 1.4%, the RBC fraction that could be removed passively through flow-splitting (i.e., without introducing the electrokinetic effects). The RBCs were further removed through sedimentation at the collection reservoirs, but the impurity levels in the fraction collected without the electrokinetic effects were increased by >5-fold, which was adequately high to alter the clear appearance of the extracted fraction (device off, Figure 5b). As mentioned above, the purity evaluation is independent of the dilution ratio. However, lowering the dilution ratio increases the hematocrit level beyond the capacity of the current design and thus degrades the purity (Table S-4).

Quality of the Extract. A valid concern regarding ETF-based blood plasma isolation is that the heat generated in the process could potentially trigger hemolysis of RBCs and/or protein denaturation. Hemolysis contaminates plasma with inhibitors released from ruptured RBCs that might interfere with downstream immunoassays or polymerase chain reactions, and thus prevent the effective detection of target proteins or nucleic acids. Conversely, denaturation causes proteins to lose their distinct native conformation and associated function, and this hinders, in particular, the diagnostic tests used for assaying plasma proteins for specific biological activities.

The visual indicator of hemolysis is the reddish appearance of harvested fraction that results from the hemoglobin contamination from ruptured cells. The fraction obtained from the device presented here did not appear reddish and emerged nearly as clean as the plasma obtained from conventional centrifugation and sedimentation (Figure 5b). Moreover, Figure 6a shows that the absorbance spectra of these extracts are devoid of any peak, particularly around 541 and 576 nm, the wavelengths that correlate well with the free hemoglobin level.[38] This contrasts with the spectra of the plasmas obtained from whole blood that was subjected to hemolytic stress (e.g., exposure to heat or hypotonic shock) before centrifugation. In the case of heat-induced stress, the peaks appeared small and further diminished with an increase in temperature, which is likely due to the thermal denaturation of hemoglobin. Although discoloration might raise concerns regarding undetected
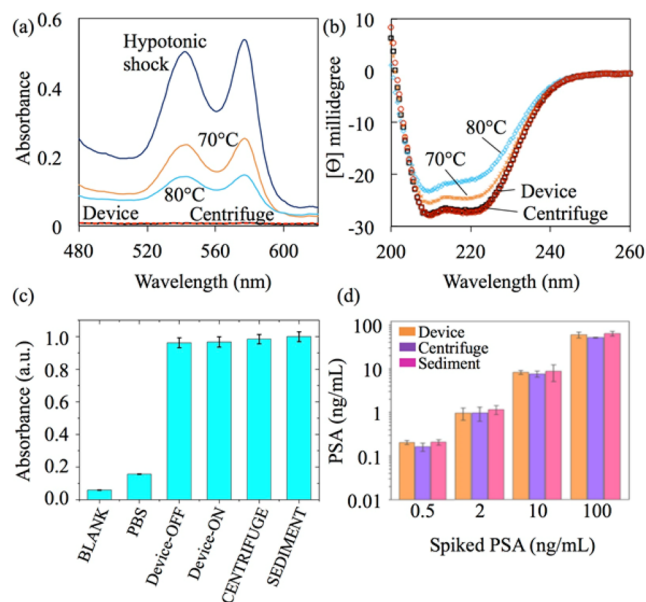
Figure 6. Comparison of the quality and utility of extracts obtained using the device and using conventional methods. (a) Absorbance and (b) CD spectra used for assessing hemolysis and protein denaturation, respectively. Heat treatments were applied for 20 s to (a) whole blood or (b) plasma extracted through centrifugation. The device treatment was performed at a flow rate of 0.05 mL/h and a peak voltage of ± 10 V_p at 650 kHz. (c) Total protein recovery based on BCA colorimetric protein assay. (d) Validation of the utility of the extracts obtained by using the ELISA for PSA.

hemolysis, the temperature at which discoloration occurs (see Figure S-8) falls above the peak temperature predicted by the simulations.

The extent of protein denaturation in harvested fraction can be evaluated by obtaining circular dichroism (CD) spectra and measuring the intensity change at a specific wavelength: the CD intensity at 222 nm ($[\theta]_{222}$), in particular, is associated with the α-helix content of proteins, and a reduction in $[\theta]_{222}$ suggests a loss of helicity and damage to the ordered protein structure.[39] The CD spectra of the plasmas obtained from centrifugation and sedimentation (not shown), and of the device extract under the stated operating conditions appeared nearly identical (Figure 6b). By comparison, $[\theta]_{222}$ was substantially decreased in the case of the plasma exposed to 80 °C for 20 s after isolation through centrifugation. This duration is comparable to the residence time of plasma proteins in the device. However, for the same duration, the spectra of the plasmas exposed to ≤ 60 °C exhibited no noticeable deviation from the spectra of unheated samples; the intensity reduction became detectable near 70 °C and increased with an increase in temperature or the duration of heat exposure (Figure S-9). This further confirms the prediction that the peak temperature within the device is below 50 °C.

The aforementioned results revealed no sign of hemolysis or protein denaturation, and thus they suggest that the heat generated in the process, although sufficient for inducing an effective ETF for harvesting blood plasma, is at a level that raises no major concern regarding plasma quality for downstream applications.

Biomarker Detection. In validating the utility of harvested fraction, a further concern is related to the recovery efficiency of target molecules. The results of the bicinchoninic acid

(BCA) protein assay, shown in reference to sedimentation in Figure 6c, reveal that the total protein recovery yield for the device extract was 96.7% $\pm$ 3.1% with the activation voltage on (± 10 V_p at 650 kHz) and 96.2% $\pm$ 3% with the activation voltage off, comparable to the level achievable in the plasma obtained with centrifugation, 98.5% $\pm$ 2.9% ($n = 4$). In the voltage-off case, the device extract was centrifuged to deplete blood cells and, for consistency, this step was also applied in the voltage-on case. Further, the results of an enzyme-linked immunosorbent assay (ELISA) showed that the levels of prostate-specific antigen (PSA) measured in the device extract and the plasmas extracted using conventional methods were comparable and exhibited a similar trend as did the levels of PSA spiked into blood samples of female donors over a broad clinically relevant concentration range (0.5–100 ng/mL) (Figure 6d). However, regardless of the plasma extraction method used, the measured PSA levels represented only about 60% of the spiked PSA levels; this corroborates previous studies reporting 30%–40% loss in immunoreactivity of spiked PSA in female serum due to PSA complex formation.[40]

CONCLUSION

We have demonstrated a novel microfluidic device for blood plasma extraction based on ETF. ETF has been introduced for the first time for the application of plasmapheresis, achieving yield and purity levels that exceed those reported for most microdevices based on electrokinetic effects (e.g., electroosmosis, DEP). The potential of the device extract has been validated through analytical measurements and PSA assaying at clinically relevant levels. The results warrant further optimization of the device to enable plasmapheresis from whole blood at a normal hematocrit level without a dilution. This will be realized by tailoring the cross-sectional profile of the channel such that the capacity of the cell-enriched layer is enhanced in relation to the sidewall undercuts, which set the characteristic size of the ETF rolls. The device is also first of its kind to introduce the depth profile of bulk microelectrodes, in addition to their layout, as a design feature for an enhanced functionality. Once optimized, the plasmapheresis device will be further integrated into a point-of-care biomarker detection microsystem.

ASSOCIATED CONTENT

S Supporting Information

The Supporting Information is available free of charge on the ACS Publications website at DOI: 10.1021/acs.analchem.6b00215.

> Theory, detailed experimental procedures, descriptions of movies, and supplementary figures and tables (PDF)
> Video microscopy of 1 μm fluorescent particles in PBS loaded in the device channel (AVI)
> Video microscopy of blood cells suspended in PBS loaded in the device channel (AVI)
> Video microscopy of blood cells moving through the junction as the blood sample is continuously supplied at a flow rate of 0.05 mL/h (AVI)

AUTHOR INFORMATION

Corresponding Author
*Phone: +852-2358 7068. Fax: +852-2358 1485. E-mail: eelyobas@ust.hk.

Notes

The authors declare no competing financial interest.

REFERENCES

(1) Jain, K. K. *The Handbook of Biomarkers*; Springer: New York, 2010.

(2) Stegmayr, B. G. *Transfus. Apher. Sci.* **2005**, *32*, 209−220.

(3) Kersaudy-Kerhoas, M.; Sollier, E. *Lab Chip* **2013**, *13*, 3323−3346.

(4) Zhang, X.; Wu, Z.; Wang, K.; Zhu, J.; Xu, J.; Xia, X.; Chen, H. *Anal. Chem.* **2012**, *84*, 3780−3786.

(5) Thorslund, S.; Klett, O.; Nikolajeff, F.; Markides, K.; Bergquist, J. *Biomed. Microdevices* **2006**, *8*, 73−79.

(6) Huang, L. R.; Cox, E. C.; Austin, R. H.; Sturm, J. C. *Science* **2004**, *304*, 987−990.

(7) Dimov, I. K.; Basabe-Desmonts, L.; Garcia-Cordero, J. L.; Ross, B. M.; Ricco, A. J.; Lee, L. P. *Lab Chip* **2011**, *11*, 845−850.

(8) Ji, H. M.; Samper, V.; Chen, Y.; Heng, C. K.; Lim, T. M.; Yobas, L. *Biomed. Microdevices* **2008**, *10*, 251−257.

(9) Son, J. H.; Lee, S. H.; Hong, S.; Park, S. M.; Lee, J.; Dickey, A. M.; Lee, L. P. *Lab Chip* **2014**, *14*, 2287−2292.

(10) VanDelinder, V.; Groisman, A. *Anal. Chem.* **2006**, *78*, 3765−3771.

(11) Davis, J. A.; Inglis, D. W.; Morton, K. J.; Lawrence, D. A.; Huang, L. R.; Chou, S. Y.; Sturm, J. C.; Austin, R. H. *Proc. Natl. Acad. Sci. U. S. A.* **2006**, *103*, 14779−14784.

(12) Choi, S.; Park, J. K. *Lab Chip* **2007**, *7*, 890−897.

(13) Faivre, M.; Abkarian, M.; Bickraj, K.; Stone, H. A. *Biorheology* **2006**, *43*, 147−159.

(14) Yang, S.; Undar, A.; Zahn, J. D. *Lab Chip* **2006**, *6*, 871−880.

(15) Mach, A. J.; Di Carlo, D. *Biotechnol. Bioeng.* **2010**, *107*, 302−311.

(16) Lenshof, A.; Ahmad-Tajudin, A.; Järås, K.; Swärd-Nilsson, A.-M.; Åberg, L.; Marko-Varga, G.; Malm, J.; Lilja, H.; Laurell, T. *Anal. Chem.* **2009**, *81*, 6030−6037.

(17) Nilsson, A.; Petersson, F.; Jonsson, H.; Laurell, T. *Lab Chip* **2004**, *4*, 131−135.

(18) Liu, C.; Stakenborg, T.; Peeters, S.; Lagae, L. *J. Appl. Phys.* **2009**, *105*, 102014−102025.

(19) Nakashima, Y.; Hata, S.; Yasuda, T. *Sens. Actuators, B* **2010**, *145*, 561−569.

(20) Jiang, H.; Weng, X.; Chon, C. H.; Wu, X. D.; Li, D. Q. *J. Micromech. Microeng.* **2011**, *21*, 085019.

(21) Chen, C.-C.; Lin, P.-H.; Chung, C.-K. *Lab Chip* **2014**, *14*, 1996−2001.

(22) Pethig, R. *Biomicrofluidics* **2010**, *4*, 022811.

(23) Castellanos, A.; Ramos, A.; González, A.; Green, N. G.; Morgan, H. *J. Phys. D: Appl. Phys.* **2003**, *36*, 2584−2597.

(24) Sigurdson, M.; Wang, D.; Meinhart, C. D. *Lab Chip* **2005**, *5*, 1366−1373.

(25) Feldman, H. C.; Sigurdson, M.; Meinhart, C. D. *Lab Chip* **2007**, *7*, 1553−1559.

(26) Sin, M. L. Y.; Liu, T.; Pyne, J. D.; Gau, V.; Liao, J. C.; Wong, P. K. *Anal. Chem.* **2012**, *84*, 2702−2707.

(27) Ouyang, M.; Mohan, R.; Lu, Y.; Liu, T.; Mach, K. E.; Sin, M. L. Y.; McComb, M.; Joshi, J.; Gau, V.; Wong, P. K.; Liao, J. C. *Analyst* **2013**, *138*, 3660−3666.

(28) Park, S.; Koklu, M.; Beskok, A. *Anal. Chem.* **2009**, *81*, 2303−2310.

(29) Gao, J.; Sin, M. L. Y.; Liu, T.; Gau, V.; Liao, J. C.; Wong, P. K. *Lab Chip* **2011**, *11*, 1770−1775.

(30) Gao, J.; Riahi, R.; Sin, M. L. Y.; Zhang, S.; Wong, P. K. *Analyst* **2012**, *137*, 5215−5221.

(31) Yobas, L.; Sharma, R. K.; Nagarajan, R.; Samper, V. D.; Naidu, P. S. R. *J. Micromech. Microeng.* **2005**, *15*, 386−393.

(32) Yobas, L.; Martens, S.; Ong, W. L.; Ranganathan, N. *Lab Chip* **2006**, *6*, 1073−1079.

(33) Xing, X.; Zhang, M.; Yobas, L. *J. Microelectromech. Syst.* **2013**, *22*, 363−371.

(34) Xing, X.; Poon, R. Y. C.; Wong, C. S. C.; Yobas, L. *Biosens. Bioelectron.* **2014**, *61*, 434−442.

(35) Xing, X.; Yobas, L. *Analyst* **2015**, *140*, 3397−3405.

(36) Hart, D. P. *Exp. Fluids* **2000**, *29*, 13−22.

(37) Gao, Z.; Agarwal, A.; Trigg, A. D.; Singh, N.; Fang, C.; Tung, C.-H.; Fan, Y.; Buddharaju, K. D.; Kong, J. M. *Anal. Chem.* **2007**, *79*, 3291−3297.

(38) Al-Soud, W. A.; Rådström, P. *J. Clin. Microbiol.* **2001**, *39*, 485−493.

(39) Saito, M.; Taira, H. *Agric. Biol. Chem.* **1987**, *51*, 2787−2792.

(40) Lilja, H.; Christensson, A.; Dahlen, U.; Matikainen, M. T.; Nilsson, O.; Pettersson, K.; Lovgren, T. *Clin. Chem.* **1991**, *37*, 1618−1625.